aerospace

MDPI

Article

On-Orbit Performance Analysis of Lithium-Ion Batteries Based on NCA System for MEO Satellites

Chenjie Kong [1,2,3], Huan Liu [2,3,*], Baojun Lin [2,3], Shaoqian Li [2,3], Qiang Zhang [2,3] and Shaohua Jia [2,3]

[1] School of Astronautics, Nanjing University of Aeronautics and Astronautics, Nanjing 210016, China; kongcj@microsate.com
[2] Shanghai Engineering Center for Microsatellites, Shanghai 201304, China; linbaojun@aoe.ac.cn (B.L.); lisq@microsate.com (S.L.); zhangq@microsate.com (Q.Z.); jiash@microsate.com (S.J.)
[3] Innovation Academy for Microsatellites of Chinese Academy of Sciences, Shanghai 201304, China
* Correspondence: liuhuan@microsate.com

Abstract

Faced with the complex space electromagnetic environment, the long solar illumination periods of medium-Earth-orbit (MEO) satellites, and the unique operating limitation under which the batteries operate under shallow charge–discharge cycles, this paper proposes a dedicated life evaluation method suitable for MEO satellite batteries. The proposed method quantifies battery performance degradation by analyzing the statistical correlation between the discharge capacity and discharge cut-off voltage during eclipse phases. Using seven years of on-orbit-measured data covering 14 eclipse seasons, we build prediction models for the cut-off voltage via Random Forest and XGBoost, with the eclipse season index and discharge capacity set as model input features. The mean squared error (MSE) of both models is lower than 0.003, demonstrating the high reliability of the modeling framework. Under the condition of a fixed discharge capacity, no obvious battery degradation exceeding the measurement uncertainty is detected within the observation period. The magnitude of potential voltage degradation is comparable to or even smaller than the 2 mV acquisition uncertainty, such that no measurable degradation phenomenon can be identified in the available dataset. At present, long-term on-orbit-measured data of MEO satellite batteries are scarce in engineering research. This study provides valuable full-measurement data support for the optimized design, autonomous on-orbit management, and life evaluation of NCA lithium-ion batteries and fills the gap in long-term on-orbit datasets for MEO satellite power systems.

Keywords: lithium-ion battery; on-orbit performance; cut-off discharge voltage; prediction; MEO

Check for updates

Academic Editor: James 'Chris' Thomas

Received: 3 June 2026
Revised: 25 July 2026
Accepted: 1 August 2026
Published: 3 August 2026

Copyright: © 2026 by the authors. Licensee MDPI, Basel, Switzerland. This article is an open access article distributed under the terms and conditions of the Creative Commons Attribution (CC BY) license.

1. Introduction

Medium Earth orbit (MEO, 2000–35,786 km) lies within the Van Allen radiation belts, characterized by a complex and dynamic space electromagnetic environment. The flux of high-energy charged particles (protons, electrons) in this orbit is significantly higher than that in low Earth orbit (LEO). Meanwhile, MEO satellites exhibit distinct "periodic shallow discharge" during eclipse seasons, coupled with long idle periods (approximately 9–10 months of illumination annually)—a stark contrast to the "high-frequency deep cycling" operating conditions of LEO satellites [1–5]. These unique characteristics result in battery degradation mechanisms (e.g., radiation-dominated interface damage, voltage

decay patterns under low depth of discharge (DOD)) that differ from those in other orbits, necessitating targeted ground simulation tests and on-orbit monitoring. However, constructing test platforms that replicate MEO's real-world environment (such as high-energy proton radiation simulators and periodic thermal cycling systems) is costly and time-consuming, which objectively limits the advancement of relevant research [6,7].

Despite the prominent strategic value of MEO satellites, there remain significant gaps in current research on their batteries. First, MEO satellites typically have a design life of 8–15 years, and complete lifecycle data for batteries require long-term accumulation—this further leads to a scarcity of publicly available data for analysis and a lack of foundational materials for literature studies [8–10]. Second, early aerospace research primarily focused on LEO, but LEO satellite batteries face acute lifespan issues due to frequent deep cycling [11]. In contrast, MEO satellite batteries are designed with radiation resistance to achieve long lifespans, and no large-scale failure issues have emerged in the short term—thus, the lifespan analysis of MEO batteries has long been a "weak area" of research. Third, traditional battery lifespan assessment relies on "full charge–discharge capacity measurement" and "high-current excitation internal resistance measurement" [12,13]. However, MEO satellite batteries cannot achieve full charge–discharge due to their "long illumination periods and shallow discharge during eclipse seasons" [14]; moreover, stringent on-orbit constraints (e.g., avoiding additional current excitation for full charge–discharge to prevent disrupting the satellite power supply) render traditional methods ineffective [15,16]. There is an urgent need to develop non-intrusive assessment methods, but verifying these new methods requires long-term on-orbit data. The lack of mature theoretical frameworks and experimental validation systems in the early stages has raised research barriers, further limiting the output of the relevant literature.

To address the technical challenge of incomplete charge–discharge testing for MEO satellite batteries, researchers have developed various capacity assessment techniques suitable for partial charge–discharge conditions. The core idea of these techniques is to establish a correlation between the battery's capacity and its characteristic parameters during partial charge–discharge processes, thereby enabling indirect capacity estimation. Methods based on incremental capacity analysis (ICA) calculate the ratio of capacity change to voltage change (dQ/dV) during battery charge–discharge to construct incremental capacity curves. Their key value lies in converting the internal electrochemical changes of the battery into observable curve features, enabling the estimation of the health states of satellite batteries [17]. However, this method requires uniform telemetry data and imposes high demands on the quality of on-orbit data. Improved equivalent circuit models represent another important technical approach. Researchers have integrated empirical models into standard equivalent circuit models to enhance the accuracy of modeling constant-current discharge processes. By developing parameter lookup tables, they simulate the complete discharge process using on-orbit partial discharge data, realizing the virtual execution of the battery pack's full discharge process and thus estimating the battery pack's capacity [18]. This method is particularly suitable for specific operating conditions in space applications and can achieve high-precision capacity estimation under partial charge–discharge conditions. Nevertheless, the establishment of empirical models has certain limitations. Data-driven machine learning has become the mainstream technical route for battery degradation prediction in recent years, and a series of standardized open-source platforms and advanced deep learning frameworks have been proposed to unify data processing and model benchmarking. Zhang et al. proposed BatteryML, an open-source unified machine learning platform for battery degradation modeling, at ICLR 2024; it integrates standardized data reading, multi-type feature extraction, mainstream traditional machine learning and deep learning model libraries (Random Forest, XGBoost,

CNN, LSTM, Transformer), and standardized evaluation metrics such as the MSE, RMSE, and R2. BatteryML unifies heterogeneous battery cycling data from multiple public datasets (MATR, CALCE, NCA/SNL, etc.) into a universal BatteryData data structure and provides configurable pipeline interfaces to realize the end-to-end training and prediction of battery SOH, SOC, and remaining useful life (RUL) tasks, greatly lowering the reproduction threshold of data-driven battery research [19].

On this basis, Zhang et al. further proposed BatLiNet, an inter-cell contrast deep learning framework published in *Nature Machine Intelligence* in 2025, which innovatively introduces an inter-cell learning auxiliary task beyond single-cell intra-cycle feature extraction. BatLiNet simultaneously learns the aging difference between target cells and reference cells and fuses single-cell aging characteristics and cross-cell comparative information through shared linear layers, which significantly reduces the prediction error under multi-material and multi-aging mixed datasets. It realizes effective transfer learning under the condition of insufficient samples of new battery systems [20].

In data-driven battery lifetime prediction, Li et al. put forward a chemistry-aware machine learning framework combining condition simulation, batch electrochemical tests, and interfacial characterization. They used HMM to reproduce US06 random vehicle loads and collected massive wide-temperature cycling data from graphite-based cells. An automatic polynomial-scale feature space was built from raw electrical signals to predict the battery life and capacity knee points. Combined with XPS results for cycled cells, six SEI aging modes were summarized to interpret internal degradation non-invasively. Moreover, the study found that Random Forest and XGBoost have favorable accuracy and interpretability under variable working conditions, which corroborates the modeling strategy adopted in this work [21].

Traditional ensemble tree algorithms including Random Forest and XGBoost are still the most reliable lightweight solutions for satellite on-orbit prediction tasks with limited data and strict real-time constraints, and they have been widely verified in existing battery prediction research. These algorithms capture the trends in battery health state changes over time by learning the input–output relationships of batteries under different operating conditions.

This section distinguishes the present work from existing studies on partial-cycle battery health evaluation and elaborates on the incremental contributions of this research from engineering data and methodological perspectives.

1. Supplementary value of rare long-term on-orbit MEO measurement data

Most existing prediction models for partial-cycle batteries are trained and validated based on ground cycling experiments, electric vehicle operating data, or LEO satellite datasets featuring frequent deep discharge cycles. These research scenarios support standardized full charge–discharge calibration and complete full-capacity observation records. In contrast, MEO satellites experience annual idle illumination windows of 9–10 months, with the maximum depth of discharge limited below 40% during eclipse seasons. Full charge–discharge calibration cannot be implemented due to on-board power constraints. Long-term continuous telemetry covering multiple eclipse cycles is rarely published in the open literature. Based on seven years of orbital operation records for the target satellite, this paper provides a complete dataset covering 14 eclipse seasons for NCA battery packs, which can serve as supplementary real orbital samples for relevant research on MEO power systems.

2. Improved partial-cycle evaluation framework adapted to MEO on-orbit constraints

Traditional partial-diagnostic methods such as incremental capacity analysis and offline equivalent circuit fitting generally require intact full voltage–capacity curves or

adjustable auxiliary excitation currents. Additional electrical interference would disrupt the satellite power bus, making these techniques difficult to deploy for long-term in-orbit monitoring. This paper establishes an evaluation framework based on the cut-off discharge voltage and discharge capacity that only utilizes native telemetry generated during routine eclipse discharge without extra current excitation, better matching the actual operating limits of MEO spacecraft.

The majority of existing AI-based battery prediction models fit capacity degradation trends using complete full-cycle laboratory data. In contrast, the Random Forest and XGBoost models constructed in this study are trained purely on natural shallow discharge data collected on orbit. Moreover, a multi-layer verification chain is constructed to suppress extrapolation bias, including physical linear degradation baseline correction, leave-one-eclipse-season-out cross-validation, and bootstrap-based uncertainty quantification.

With reference to the existing research context, this study explores an MEO satellite case and attempts to address several underexplored aspects through two main efforts.

Supplementary data work: This study compiles complete on-orbit data from an MEO satellite battery over 7 years (covering 14 eclipse seasons), with the expectation of providing additional material for use in future research, addressing the relatively limited measured data accumulation in this field. In addition, results from 700 full charge–discharge cycles in ground tests show capacity degradation of approximately 3%, and this observation may help to improve the understanding of cycling stability.

A reference perspective on assessment methods: This paper presents a reference indicator for observing battery lifespan degradation, namely the change in the discharge cut-off voltage at the maximum discharge capacity during the deepest eclipse phase. A decrease in this voltage to 3 V per cell (with nine cells in series, corresponding to 27 V for Pack A) may serve as one reference basis for determining whether the battery is approaching its end of life. This threshold of 27 V is selected based on ground-measured SOC–voltage data, as detailed in the Table 1 below.

Table 1. Measured SOC–voltage characteristics of NCA battery pack.

Operating Condition	SOC = 100%	SOC = 90%	SOC = 80%	SOC = 70%	SOC = 60%	SOC = 50%
Open-Circuit (Pack, V)	36.85	35.87	35.08	34.39	33.49	32.89
Open-Circuit (Cell, V)	4.09	3.99	3.90	3.82	3.72	3.65
0.5C Discharge (Pack, V)	36.88	35.21	34.34	33.63	32.88	32.26
0.5C Discharge (Cell, V)	4.04	3.92	3.82	3.74	3.66	3.59
0.1C Charge (Pack, V)	36.90	36.11	35.28	34.60	33.76	33.13
0.1C Charge (Cell, V)	**4.10**	**4.01**	**3.92**	**3.85**	**3.75**	3.68
Operating Condition	**SOC = 40%**	**SOC = 30%**	**SOC = 20%**	**SOC = 10%**	**SOC = 0%**	
Open-Circuit (Pack, V)	32.45	32.06	31.39	30.05	27.00	
Open-Circuit (Cell, V)	3.61	3.56	3.49	3.39	3.00	
0.5C Discharge (Pack, V)	31.72	31.27	30.68	29.83	27.00	
0.5C Discharge (Cell, V)	3.53	3.48	3.42	3.32	3.00	
0.1C Charge (Pack, V)	32.68	32.31	31.68	30.83	28.10	
0.1C Charge (Cell, V)	3.63	3.59	3.52	3.43	3.13	

Battery topology: Each pack is configured with nine cells in series per string and three parallel strings (3P9S), with nine NCA single cells connected in series within each string.

Failure criterion basis: Under open-circuit and 0.5C discharge states, a single-cell voltage of 3 V corresponds to zero residual SOC, representing the full depletion of the cell. To avoid irreversible degradation induced by over-discharge, 3 V is defined as the end-of-life threshold for individual cells.

Derivation of pack failure threshold: Each string consists of nine series-connected cells. If any single cell drops to 3 V during discharge, the total terminal voltage of the pack will reach 9 × 3 V = 27 V, which is judged as the end-of-life state.

In summary, this paper integrates multi-year on-orbit telemetry, ground accelerated aging tests, and an adaptable non-intrusive lifetime prediction model to form a complete analytical framework for MEO NCA batteries. The proposed workflow can serve as a reference for the lifetime evaluation of satellites in the same orbit and mitigate the scarcity of measured orbital data in existing research.

2. Materials and Methods

2.1. Long-Life Management Strategy for On-Orbit Batteries in MEO Satellites

The MEO satellite battery system described in this paper adopts two parallel-connected battery packs for power supply. Each cell is a 25 Ah NCA lithium-ion battery, and the battery packs (75 Ah each) are configured in a "3P9S" structure. For the long-life design of on-orbit batteries, the temperature range of the battery packs is controlled within 0 −+ 15 °C during the idle period in illumination seasons, and the temperature difference between individual cells in a battery pack is kept below 3 °C. Three days before the satellite enters the eclipse season, the battery packs are heated according to the eclipse temperature threshold, with their temperature range controlled within 15–25 °C to facilitate charge–discharge operations during the eclipse season.

During the long illumination season, the battery packs are in an idle state with a state of charge (SOC) of 70%. If the battery pack voltage is detected to be lower than 34.2 V (3.80 V per cell), a supplementary charging operation is performed on the batteries. The charging method uses a small current of 1 A (the standard recommends a supplementary charging current of 0.01 C–0.02 C), and charging stops when the battery pack voltage reaches 35.1 V (3.90 V per cell). During the eclipse season, the battery packs are fully charged using a "constant current followed by constant voltage" control mode: first, constant-current charging is conducted at 4 A; when the charging cut-off voltage reaches 36.45 V, the mode switches to constant-voltage charging; charging stops when the charging current is less than 0.25 A for 20 consecutive frames. This long-life management measure is proposed in accordance with the GJB9741-2020 Specification for Lithium-Ion Battery Packs of Spacecraft [22].

Under the operation of this long-life management strategy, the temperature, voltage, and charge–discharge current of the MEO satellite's battery packs during one eclipse season are as shown in Figure 1 below.

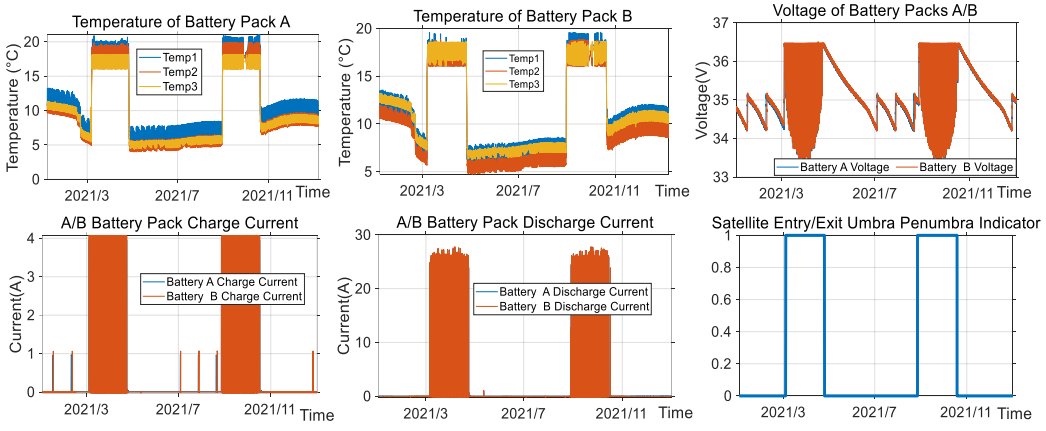


Figure 1. Satellite battery pack: temperature and electrical parameter graphs (one eclipse season).

For the satellite's entry/exit shadow flag in Figure 1, 1 represents the eclipse season and 0 represents the sunlight season. As can be seen from the figure, the satellite temperature remains within the threshold setting range regardless of whether it is in the sunlight season or the eclipse season, which meets the design requirements of the long-life management strategy.

Specifically, the satellite performs large-load charging and discharging operations during the eclipse season, while it mainly relies on self-discharging and trickle charging during the sunlight season. When the battery voltage drops to the lower limit of the storage voltage due to self-discharging, the system will automatically start a 1 A small-current supplementary charging process. Statistics show that a total of 6 supplementary charging operations were completed during the sunlight season within one year.

According to the GJB 9741-2020 Specification for Lithium-Ion Battery Packs of Spacecraft, the maximum design depth of discharge (DOD) for batteries used in high-orbit satellites should not exceed 80%. However, this 80% DOD adopted in the design takes into account the scenario whereby one battery cell fails at the end of the service life. In the actual on-orbit operation of the satellite, the depth of discharge generally does not exceed 40%. Therefore, for medium- and high-orbit satellites, the batteries always operate under shallow charge–discharge cycles.

2.2. Introduction to the Random Forest Algorithm

Random Forest is an ensemble-based supervised regression/classification algorithm that is widely adopted for battery state prediction and fault diagnosis [23–25]. Its core dual-randomization design (random sample bootstrap sampling + random feature subset selection) effectively mitigates single decision tree overfitting [26–28]. Unlike independent single trees, the model generates multiple sub-datasets via sampling with replacement and trains separate decision trees on limited feature pools. For regression tasks such as our battery cut-off voltage prediction task, the final output is averaged over all tree predictions to boost stability [29,30]. In this work, only two input variables (eclipse season number, discharge capacity) are adopted, so one feature is randomly selected at each node split during training.

2.3. Introduction to the XGBoost Algorithm

XGBoost is an optimized gradient boosting tree ensemble algorithm [31–35]. Differing from the parallel training pattern of Random Forest, XGBoost iteratively builds serial decision trees to compensate for the residual errors of prior models, with multiple regularization strategies embedded to relieve overfitting risks. Its core optimizations include a limited tree depth, an L2 leaf weight penalty, and the random sampling of samples/features in each iteration. In our MEO battery prediction task, we set the learning rate to 0.1, max_depth = 3, min_child_weight = 1, subsample = 0.8 and colsample_bytree = 0.8. Benefiting from high precision and strong generalization, XGBoost realizes reliable voltage validation on the 13th–14th eclipse cycles and extrapolation to the 20th end-of-life eclipse season, supporting our orbital battery lifetime evaluation.

2.4. Processing and Construction of the "Discharge Capacity–Cut-Off Discharge Voltage" Correlation Dataset

The MEO orbit satellite studied in this paper has distinct eclipse seasons and discharge characteristics: it experiences 2 eclipse seasons annually, each lasting about 30 days; the orbital period is 13 h; and one eclipse (accompanied by battery discharge) occurs per orbital period. The discharge process exhibits a "dynamic variation" feature: as the satellite's eclipse immersion depth increases, the battery's depth of discharge (DOD) gradually increases; when a single eclipse reaches the maximum duration (approximately 1 h), the

corresponding maximum discharge capacity is about 24.89 Ah; and as the satellite gradually exits the eclipse, the DOD decreases slowly.

The telemetry data downloaded from the satellite provide a basis for battery state analysis, with core data including the battery pack voltage and discharge current. Based on these data, this study first constructs a "discharge capacity–cut-off discharge voltage" correlation dataset, and the specific data processing workflow is as follows.

Data Integrity Assurance: Due to differences in the satellite's operating areas, telemetry data are transmitted via two types of data packets—data in domestic areas are directly transmitted through domestic telemetry packets with a transmission frequency of 1 packet per second; data in overseas areas are transmitted through inter-satellite links via overseas telemetry packets. To avoid data loss, it is necessary to first align the two types of data packets on the time axis and merge them, ensuring coverage of the complete eclipse discharge process. The comparison chart of the data before and after merging is shown in Figure 2 below.

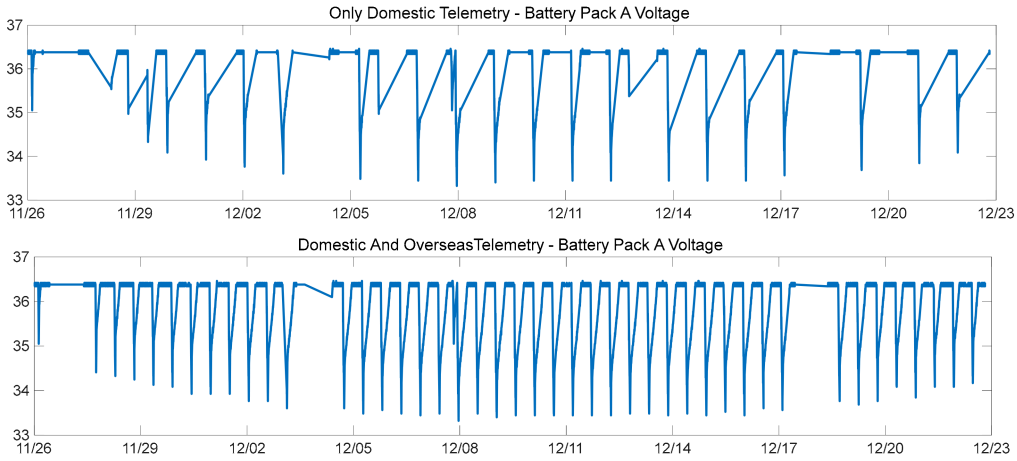


Figure 2. Comparison chart of data before and after merging.

It can be seen that, after merging, the number of charge–discharge cycles in the data increases and the data integrity is enhanced. However, a small amount of data is lost in individual cycles due to issues such as link transmission and data transfer; such incomplete data will be discarded during data analysis and processing.

Calculation of Key Parameters: The actual discharge capacity of each discharge process is calculated by means of integrating the discharge current over time. Meanwhile, the minimum voltage of the battery pack during the discharge process is extracted and defined as the cut-off discharge voltage corresponding to the discharge capacity, thus establishing a one-to-one correspondence between the discharge capacity and cut-off discharge voltage. The curve chart showing the relationships among the discharge capacity, cut-off discharge voltage, and discharge cycles of the satellite during one eclipse season is presented in Figure 3. A satellite experiences approximately 60 cycles in one eclipse season, and individual cycles are discarded due to incomplete data caused by problems such as link transmission and data storage. The sampling of telemetry data exhibits slight jumps affected by the accuracy of AD conversion, but this does not affect the judgment of the overall trend.

Statistical Analysis of Multi-Eclipse-Season Data: Based on the aforementioned processing, data from 14 eclipse seasons experienced by the satellite during its 7 years of on-orbit operation were cumulatively analyzed, forming a comparative dataset for multiple eclipse cycles (see Figure 4 for data distribution).

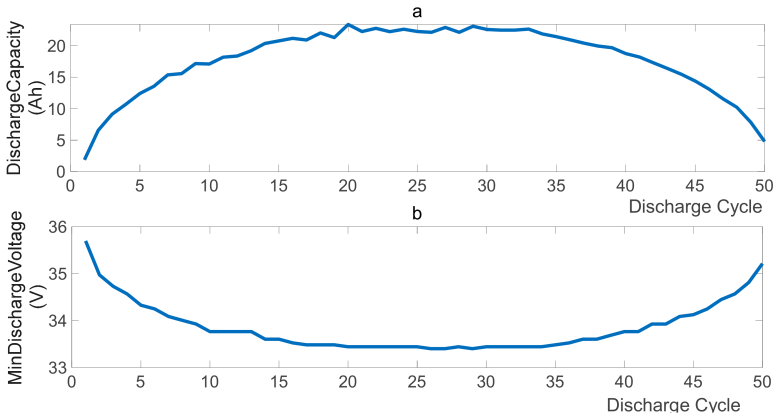


Figure 3. Discharge capacity vs. cut-off voltage and cycles (one eclipse season). (**a**) Discharge capacity curve, (**b**) Minimum discharge voltage curve.

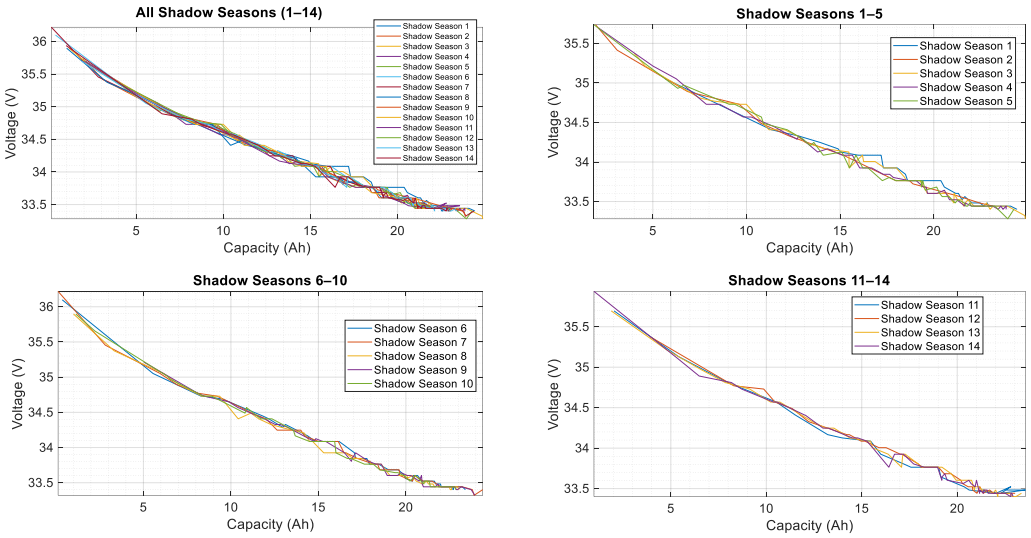


Figure 4. Battery discharge capacity vs. voltage curve.

In terms of performance prediction, the eclipse season count and discharge capacity are used as the input features of the model, and the cut-off discharge voltage is taken as the prediction target. It should be noted that, in addition to the discharge capacity, the discharge cut-off voltage is susceptible to variations in temperature and discharge current. Within the operating conditions of this study, the temperature and discharge current are maintained within relatively stable ranges, which supports the selection of the above features for modeling; nevertheless, minor fluctuations still exist within these operating bounds and exert small influences on the cut-off voltage. Two machine learning algorithms, Random Forest and XGBoost, are adopted to construct the prediction model. For details of the algorithms, refer to Sections 2.5 and 2.6.

2.5. Implementation of the Random Forest Algorithm

The implementation steps of the Random Forest algorithm are as follows.

I. Data Preparation

Data Extraction: From the "discharge capacity–cut-off discharge voltage" dataset of 14 eclipse seasons processed in the previous section, extract the eclipse season number, discharge capacity, and cut-off discharge voltage.

Data Splitting: Use the data from the first 12 eclipse seasons as the training set and the data from the last 2 seasons as the test set. Match each piece of data with its corresponding

eclipse season number to form a two-dimensional feature consisting of "eclipse season number + discharge capacity".

Standardization: Standardize the features and scale them to the [0, 1] range to eliminate differences in dimensions and avoid affecting model training.

II. Model Training and Prediction

A. Random Sample Sampling (Bootstrap Sampling)
Extract 100 independent sub-sample training sets from the original training set, where each sub-sample corresponds to the training data for one decision tree. The size of each sub-sample is consistent with that of the original training set (X_train). The samples are drawn with replacement to ensure randomness.

B. Random Feature Selection
When constructing each split node of a decision tree, instead of using all features, only 1 feature is randomly selected from the 2 features ("eclipse season number + discharge capacity") as the candidate split feature.

C. Multi-Tree Ensembling: "Averaging Method" for Regression Tasks
First, construct multiple trees: build 100 independent decision trees to form a "forest". Each tree is trained based on an independent bootstrap sub-sample; the split nodes of each tree are constructed using randomly selected features; the structure and parameters of the 100 trees are completely independent to avoid the homogenization of all trees. Then, the averaging method for regression tasks is used to integrate the results.

III. Training Validation

Split the training set into subsets at an 8:2 ratio. After training the model on the subsets according to the above steps, calculate the evaluation metrics (MSE, MAE, RMSE, R^2) using the validation set.

IV. Test Prediction

Use the trained model to predict the cut-off voltages corresponding to different discharge capacities in the last 2 eclipse seasons (the 13th–14th eclipse seasons).

The specific implementation process is shown in Figure 5 below.

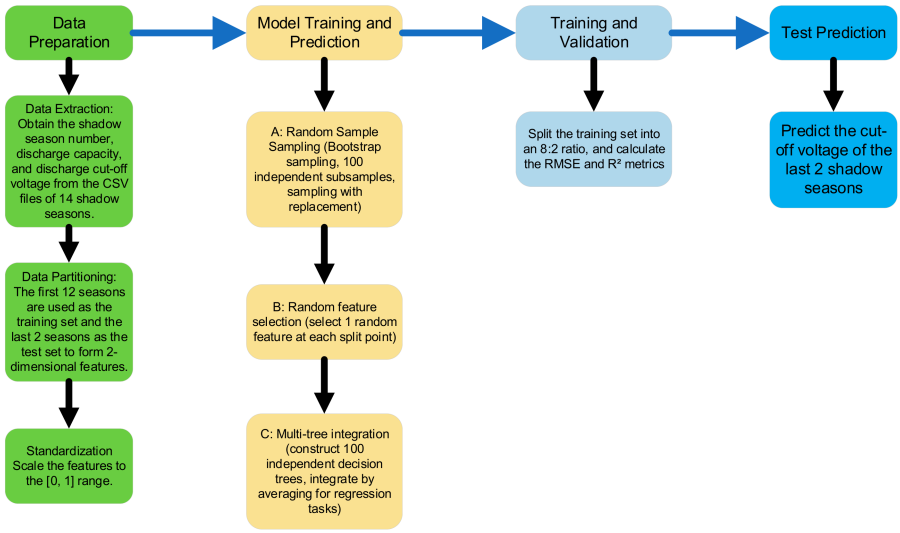


Figure 5. Random Forest algorithm-specific implementation flowchart.

2.6. Implementation of the XGBoost Algorithm

The data preparation phase of the XGBoost algorithm is identical to that of the Random Forest algorithm. The model configuration is shown in Table 2 below.

Table 2. XGBoost model configuration table.

Parameter	n_Estimators	Max_Depth	Learning_Rate	Sub-Sample	Colsample_Bytree	Random_State
Value	100	3	0.1	0.8	0.8	42

The specific algorithm implementation steps are as follows.

I. Gradient Boosting Training

Call the training set to start training; the underlying layer executes XGBoost's "iterative error optimization" logic. The detailed process is as follows.

Initial Model: Construct a simple initial model (the average voltage of all training samples) as the prediction result of the 0th round.

II. 1st Round of Iteration (Constructing the 1st Tree):

First, calculate the error gradient of the initial model.

The mean squared error (MSE) loss for a single sample in XGBoost is calculated as in Formula (1):

$$L(y, \hat{y}) = \frac{1}{2}(\hat{y} - y)^2 \quad (1)$$

where y = true value of the sample; $\hat{y}$ = predicted value of the model.

The gradient is defined as "the partial derivative of the loss function with respect to the predicted value $\hat{y}$, i.e., $\frac{\partial L}{\partial \hat{y}}$. Using the chain rule to expand and compute the derivative, we obtain $\frac{\partial L}{\partial \hat{y}} = \hat{y} - y$.

Next, take the error gradient as the new target value to train the 1st decision tree, enabling the tree to predict the error gradient (i.e., correcting the error of the initial model).

Then, assign a weight (learning_rate = 0.1) to the 1st tree and integrate the tree's prediction results into the ensemble model according to this weight. The new predicted value is calculated as follows: new predicted value = initial predicted value + (predicted value of the 1st tree $\times$ 0.1).

III. 2nd–100th Rounds of Iteration (Constructing the 2nd–100th Trees):

For the ensemble model in each round, repeat the process of "calculating error gradient $\rightarrow$ training a new tree $\rightarrow$ weight integration"; each tree focuses on correcting the error from the previous round.

Meanwhile, regularization is implemented through max_depth = 3 (limiting tree depth), sub-sample = 0.8 (sample sampling), and colsample_bytree = 0.8 (feature sampling) to prevent the trees from overfitting to the training data. The final model is the weighted integration of 100 trees, forming an ensemble model capable of outputting voltage prediction values.

IV. Model Validation (Evaluating Algorithm Generalization):

Use the validation subset to generate predicted values, and quantify the algorithm's performance through 4 evaluation metrics for regression tasks.

Mean Squared Error (MSE): Calculates the average of the squared differences between predicted values and true values, reflecting the squared magnitude of errors.

Root Mean Squared Error (RMSE): The square root of the MSE, converted back to the voltage unit (V), which more intuitively reflects the error magnitude.

Mean Absolute Error (MAE): Calculates the average of the absolute differences between predicted values and true values; it is robust to outliers.

Coefficient of Determination (R^2): Measures the ability of features to explain the target value; a value closer to 1 indicates better algorithm fitting performance.

The validation metrics are used to determine whether the algorithm is overfitting, providing a reliability basis for subsequent predictions.

V. Prediction Execution (Algorithm Output Layer):

Test Set Prediction: Call the model on the standardized feature matrix of the 13th–14th eclipse seasons to generate voltage prediction values. These values are compared with actual voltages to verify the algorithm's performance on new eclipse seasons.

Target Set Prediction: Generate prediction values for the standardized feature matrix of the 20th eclipse season and output the core prediction result of the algorithm (the battery voltage in the 20th eclipse season).

The specific implementation process is shown in Figure 6 below.

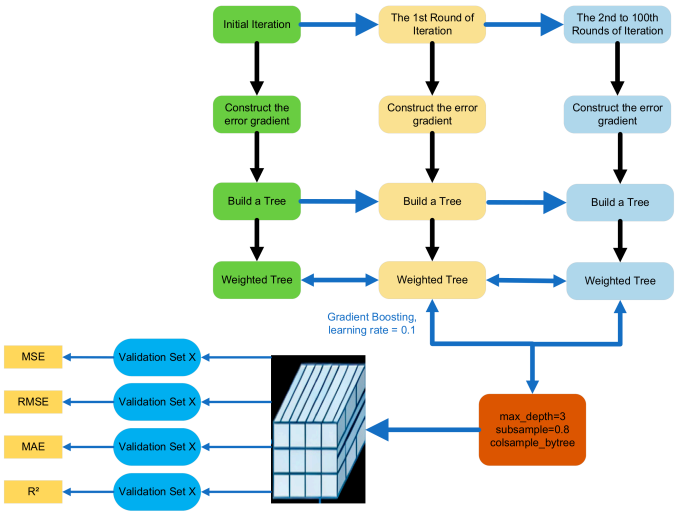


Figure 6. XGBoost algorithm-specific implementation flowchart.

3. Results and Discussion

3.1. Results

The prediction results of the two models for the 13th–14th eclipse seasons are shown in Figure 7 below. The performance metrics are presented in Table 3 below. It can be seen that both algorithms achieve excellent prediction accuracy. The residual plots are presented in Figure 8.

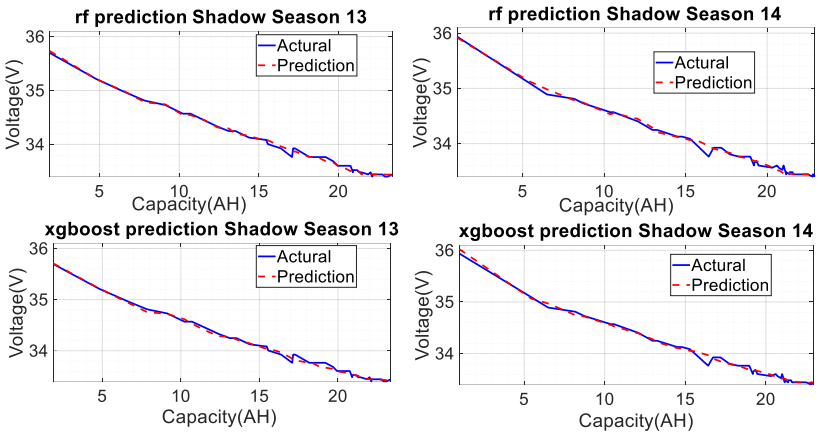


Figure 7. Prediction charts of battery voltage for shadow seasons 13–14.

Table 3. Performance indicator comparison.

	rf_Prediction _Season_13	rf_Prediction _Season_14	Xgboost_Prediction _Season_13	Xgboost_Prediction _Season_14
MSE	0.001385 V^2	0.002712 V^2	0.001512 V^2	0.002491 V^2
MAE	0.025683 V	0.036771 V	0.029164 V	0.035118 V
R^2	0.9951	0.9907	0.9946	0.9914
RMSE	0.037218 V	0.052078 V	0.038884 V	0.049913 V

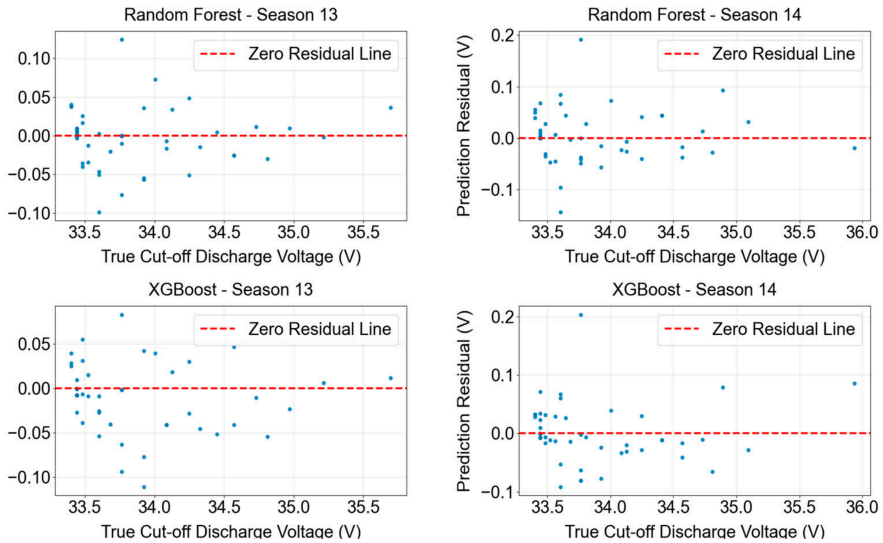


Figure 8. Residual plots under different cut-off voltages.

Using the Random Forest algorithm, the relationship curve between the battery's discharge capacity and the cut-off discharge voltage at the end of the satellite's 10-year design life (i.e., the 20th eclipse season) is predicted, as shown in Figure 9 below. It can be observed that, at the end of the satellite's service life, the battery's cut-off discharge voltage corresponding to a discharge capacity of 24.89 Ah is 33.32 V, which is higher than 27 V (the discharge voltage indicating battery failure). The on-orbit performance of the satellite battery described in this study is excellent.

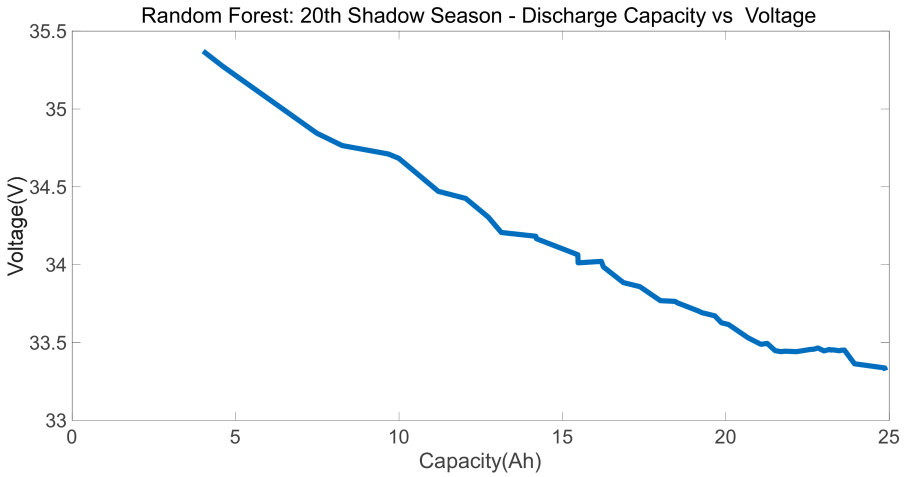


Figure 9. Relationship curve between discharge capacity and cut-off discharge voltage of satellite battery at end of 10-year service life (20th eclipse season).

3.2. Reliability Verification of Long-Term Extrapolation

To improve the rigor of the 10-year on-orbit life extrapolation, supplementary quantitative verification analyses are conducted to address the insufficient validation problem caused by merely extrapolating results via tree-based models. All analyses are quantitatively calculated based on the full measured data from the 1st to 14th eclipse seasons, as detailed below.

1. Supplementary Linear Physical Degradation Baseline Model

A linear empirical aging model is established as a physical calibration benchmark for cross-verification with machine learning extrapolation results. For the core evaluation capacity of 22.92 Ah, the measured values of the 1st and 14th eclipse seasons are adopted to calculate the average seasonal degradation slope of -0.0028 V per eclipse season. The conservatively predicted voltage extrapolated to the 20th eclipse season is 33.389 V. This value serves as a conservative calibration baseline for tree model extrapolation; it can mitigate the risk of optimistic prediction bias inherent in purely data-driven models to a certain extent. The validation results are displayed in Figure 10.

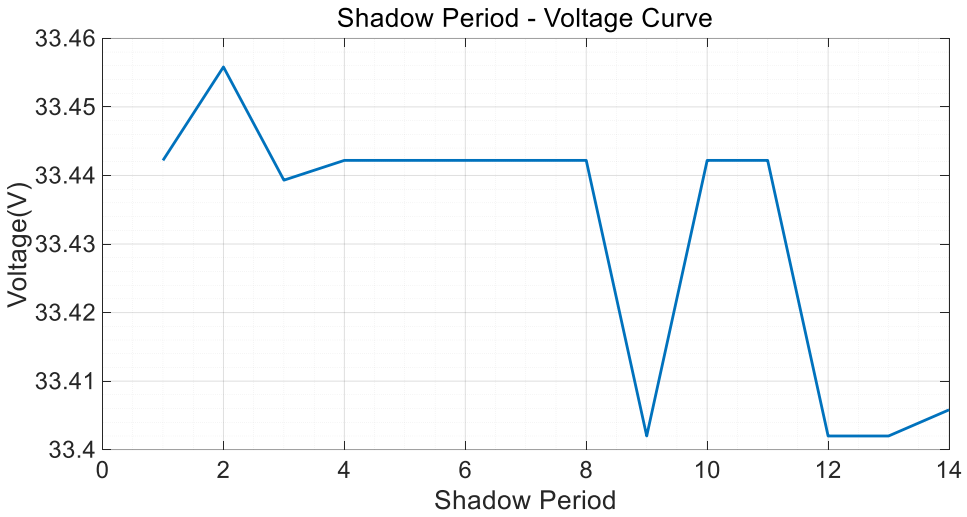


Figure 10. Trend of voltage variation with eclipse shadow period.

As illustrated in the figure, the voltage does not decrease strictly monotonically due to sampling errors, and the degradation trend cannot be distinctly identified at the current stage. Nevertheless, slight voltage degradation is observed in the 14th eclipse season compared with the initial operation period.

A 12-bit AD chip is adopted for the voltage acquisition of the satellite battery pack, with a sampling error of 2 mV. The actual degradation magnitude of the battery at present is extremely small and is lower than this sampling error threshold. Accordingly, weak degradation signals are covered by sampling errors when comparing the cut-off voltage under an identical discharge capacity, resulting in an indistinct monotonic voltage drop trend.

Considering the cumulative degradation characteristic of the battery pack over on-orbit years, continuous tracking and observation of voltage degradation trends will be carried out in follow-up work. As the satellite operates in orbit for a longer duration, battery degradation will accumulate gradually. Once the degradation magnitude exceeds the 2 mV AD sampling error threshold, the attenuation of the cut-off discharge voltage will break through the masking of sampling errors and present observable variation patterns. Long-term telemetry data will be collected and analyzed to record the voltage degradation

characteristics in this stage, so as to enrich the supporting data for long-cycle life evaluation and provide a more comprehensive reference for battery life assessment in MEO satellites.

2. Leave-One-Eclipse-Season-Out Cross-Validation

Leave-one-eclipse-season-out cross-validation, which strongly resembles the extrapolation scenario, is supplemented to evaluate the generalization performance of the model.

For the 14 sets of measured eclipse season data, one entire eclipse season is completely reserved as an independent test set that never participates in model training in each round of validation; this avoids potential data leakage, as seen in conventional cross-validation schemes. The remaining 13 eclipse seasons are used for model training. This process is repeated for all 14 eclipse seasons to cover all potential validation scenarios.

The validation covers all four discharge depth conditions adopted in this study, namely 14 Ah, 17 Ah, 20 Ah, and 22.92 Ah (near full-depth evaluation point), to verify the model performance under all operating conditions.

The validation results are displayed in Figure 11.

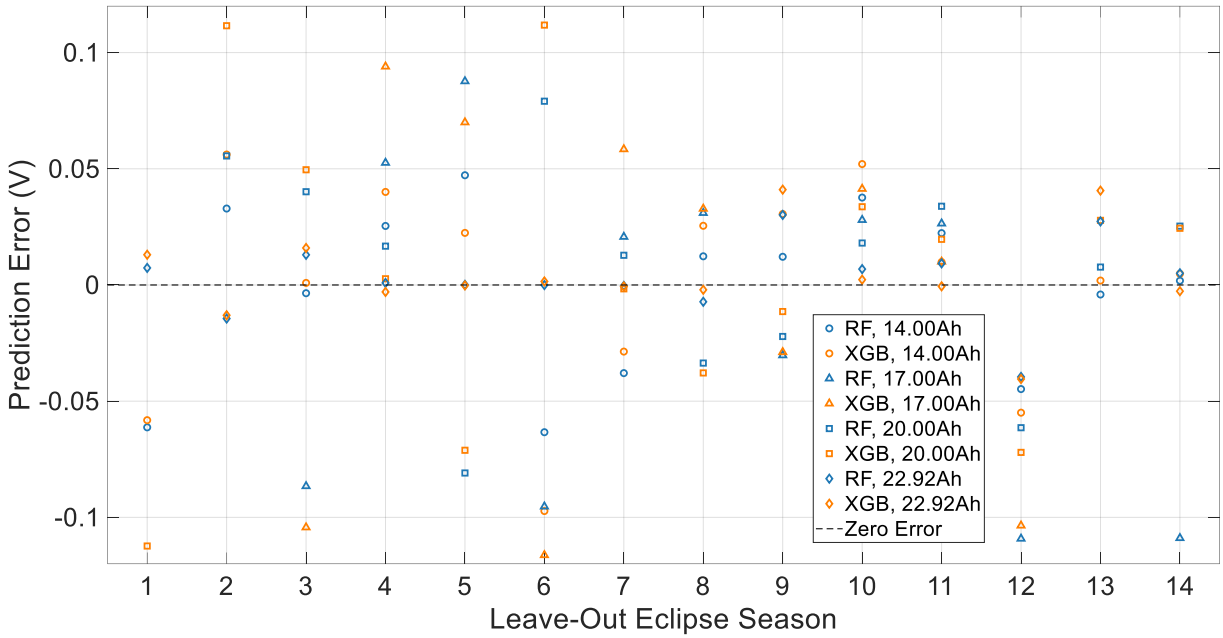


Figure 11. Leave-one-eclipse-season-out cross−validation prediction error.

From the figure, the following can be observed.

Error distribution characteristics: All prediction errors corresponding to 14 eclipse seasons and four discharge depths are constrained within a small range of [−0.12 V, 0.12 V], and most errors are extremely close to the zero-error line. Compared with the 6.4 V safety margin between the predicted minimum voltage and the 27 V end-of-life (EOL) threshold, errors of such magnitude can be neglected.

The cross-validation results sufficiently demonstrate that the proposed model can accurately predict the capacity–voltage characteristics of completely unseen eclipse seasons within the observed dataset range. It should be noted that the leave-one-eclipse-season-out cross-validation only assessed model performance within the range of existing observed eclipse seasons. This validation scheme evaluates interpolation-like predictions among known time samples and cannot fully replicate long-term extrapolation far beyond the temporal coverage of available measurements. Therefore, the favorable cross-validation performance does not guarantee equivalent prediction accuracy for the 20th eclipse season outside the observed time span.

3. 95% Prediction Confidence Intervals:

Bootstrap resampling is adopted to quantify the uncertainty of tree model extrapolation. A total of 200 independent sub-models are trained via repeated resampling, and the two-sided 95% confidence intervals of all prediction points are calculated for the full capacity range of 5–24.5 Ah in the 20th eclipse season. The detailed results are presented in Figure 12.

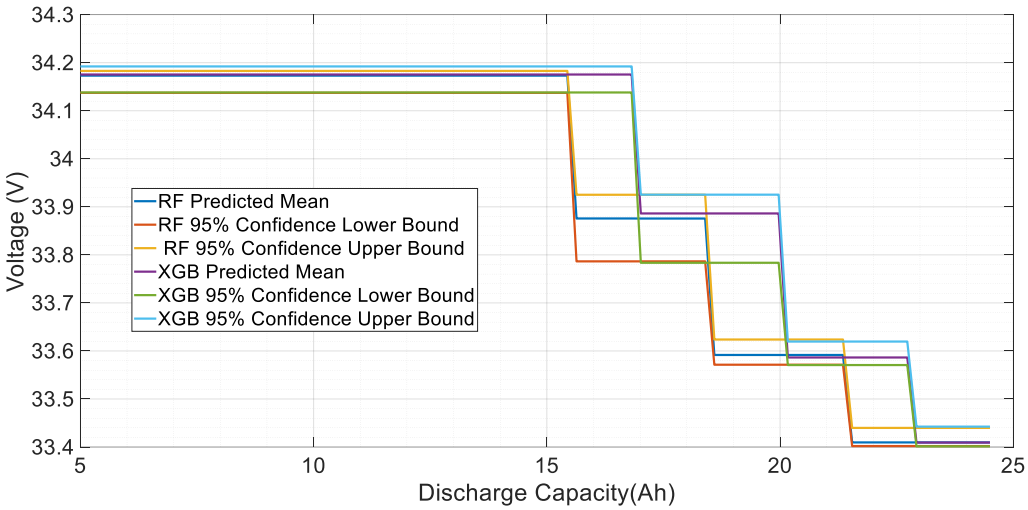


Figure 12. The 95% confidence intervals for the 20th eclipse season, full capacity.

4. Extrapolation Sensitivity Analysis

Moreover, ±5% perturbation tests are conducted on the core input features (eclipse season index, discharge capacity) to quantify the influence of input fluctuations on the prediction results.

The analysis results show that the maximum negative voltage perturbation for all key capacity points is 0 V. Minor fluctuations in input parameters cannot induce an obvious negative voltage offset, and only a minor positive voltage rise is observed under partial working conditions in the XGBoost model. It can be concluded that the extrapolation results are insensitive to minor variations in the input parameters, and no extreme offset risk is detected. The corresponding sensitivity analysis results are listed in Table 4.

Table 4. Results of sensitivity analysis.

Discharge Capacity (Ah)	RF Baseline (V)	RF Max Negative Drop (V)	RF Max Positive Rise (V)	XGB Baseline (V)	XGB Max Negative Drop (V)	XGB Max Positive Rise (V)
14	34.1758	0	0	34.1747	0	0
17	33.8865	0	0	33.9227	0	0.252037
20	33.586	0	0	33.5794	0	0.343315
22.92	33.4074	0	0	33.4052	0	0.174194

3.3. Discussion

The satellite is equipped with precise on-orbit segmented thermal control to lock temperature fluctuations within narrow, stable ranges: 0–15 °C during long illumination idle periods and 15–25 °C throughout all eclipse discharge stages. All valid comparison samples are collected under the uniform eclipse temperature window, removing temperature-induced voltage drift. Moreover, the battery is consistently maintained at the identical full SOC state before every eclipse discharge. By fixing the target discharge volume at 24.89 Ah and screening only matched telemetry records for comparison, all vari-

ations in cut-off voltage are mainly attributed to the intrinsic electrochemical degradation of NCA cells, rather than fluctuations in temperature, initial SOC, or eclipse runtime.

Compared with its initial state, obvious signs of severe degradation have not been detected from the MEO satellite battery's seven-year on-orbit telemetry data. This phenomenon can be jointly explained by three contributing factors: the inherently slow aging tendency of NCA battery materials, the reasonably optimized on-orbit operation regime, and the shielding effect brought by 12-bit AD sampling measurement noise. Relevant detailed analysis is provided as follows.

1. The inherent low-degradation characteristic of the battery system lays the foundation

The satellite adopts NCA lithium-ion cells with favorable cycle stability. Ground accelerated aging tests suggest that the cell capacity only declines by approximately 3% after 700 alternating cycles between 80% and 100% DOD, which reflects its relatively mild aging trend and indicates favorable material conditions for long-term in-orbit service.

In the ground-based accelerated life tests, a discharge current of 17.5 A and a constant charging current of 5 A were used. The single-cell battery was charged and discharged alternately at 80% and 100% depths of discharge, with a total of 700 accelerated life tests conducted. The specific capacity degradation of the single-cell battery is shown in Table 5 below.

Table 5. Capacity fading of single battery cell in ground accelerated life test.

Cycle Count	100% DOD Capacity (Ah)	Full-Charge Voltage (V)	100% DOD Voltage (V)	Compared with the Initial Capacity Decay Rate
1	25.7900	4.1959	3.0027	/
101	25.5541	4.1973	2.9868	0.9147%
201	25.5319	4.1971	2.9987	1.0008%
301	25.20915	4.1968	3.0049	2.2522%
401	25.4057	4.1965	3.0785	1.4901%
501	25.3272	4.1957	3.0246	1.7945%
601	25.1123	4.195	3.0489	2.6278%
701	25.01845	4.1948	3.0455	2.9917%

The conditions of the ground accelerated life test were as follows.

(1) Number of test samples and data selection description

Seven brand-new NCA lithium-ion single cells from the same batch were tested in parallel simultaneously in this accelerated life test. The voltage and capacity data of all seven cells were collected synchronously throughout the test. However, partial data of some cells were missing in some stages due to interruptions in equipment data acquisition, failing to form complete and continuous records covering all 700 cycles.

Therefore, only one single cell with full and uninterrupted data is included as the demonstration sample in Table 3. The capacity fading trends of the other six cells within their complete data intervals show good consistency with this selected cell. The seven cells exhibit limited dispersion in capacity degradation indicators.

(2) Ambient Temperature

The whole charge–discharge cycling test was carried out under a constant room temperature of 25 °C throughout the experiment.

(3) Charge and Discharge Rates

Constant-current charging at 0.2 C and constant-current discharging at 0.7 C were adopted, and these two current profiles were used alternately in the full cycling process.

(4) SOC Range and Cycling Profile

An alternating cycling profile with an 80% depth of discharge (DOD) and 100% DOD was adopted in the test. One complete cycle unit consisted of one charge–discharge cycle at 80% DOD followed by one cycle at 100% DOD, and this combination was repeated alternately. The charge cut-off voltage was set to 4.2 V, and the SOC of the single cell varied within the range of 0 to 100%.

2. Optimized segmented on-orbit operation regime helps to slow down battery aging progress

The satellite implements a segmented thermal matching and mild shallow charge–discharge operation scheme, which can help to mitigate the occurrence of adverse side reactions and slow the overall aging rate to a certain extent.

Discharge Aspect: There are only two eclipse seasons per year (30 days each), and the maximum depth of discharge (DOD) per cycle is $\leq$40% (far lower than the full-discharge condition in ground tests). This may reduce risks such as electrode active material peeling and interface deterioration induced by large-range lithium intercalation/deintercalation.

Temperature Aspect: The temperature is controlled at 0–15 °C during the sunlight period (to slow electrolyte oxidation) and the system is preheated to 15–25 °C before entering the eclipse (to ensure discharge stability), reducing side reactions to some degree.

Charging Aspect: A small current of 1 A (0.04 C) is used for supplementary charging, and a constant-current + constant-voltage mode with 4 A (0.16 C) is adopted for charging during the eclipse. This mild charging mode can lower the risk of SEI film rupture and lithium dendrites caused by high-current impact.

Under the above coordinated operation rules, the voltage attenuation corresponding to the fixed 24.89 Ah discharge volume remains relatively subtle within seven years of observation.

3. 12-Bit AD Sampling Error Masks Minor Degradation

A 12-bit analog-to-digital (AD) converter is adopted for on-board battery voltage acquisition, introducing a sampling error of 2 mV. If the actual in-orbit battery degradation is smaller than this sampling error threshold, subtle degradation signals will be obscured when comparing cut-off voltages at identical discharge capacities. Consequently, a clear declining voltage trend cannot be distinguished from measurement noise.

Battery degradation accumulates progressively with the in-orbit service duration. Accordingly, future work will continuously track the evolution of battery voltage degradation. As the satellite accumulates longer operating time, battery degradation will gradually build up. Once the degradation magnitude exceeds the 2 mV AD sampling error threshold, the decay of the discharge cut-off voltage will emerge from error masking and form distinguishable trends. Long-duration telemetry data should be persistently collected to characterize voltage degradation in this stage. This will enable the further evaluation of battery performance near its end of life (i.e., the 10-year design life) and deliver more comprehensive data to support long-cycle lifetime assessment for batteries aboard MEO satellites.

4. Conclusions

Addressing the operating conditions of medium-Earth-orbit (MEO) satellites—including the complex electromagnetic environment, long sunlight seasons, and shallow charge–discharge cycles of batteries—this study focuses on the on-orbit management and life assessment of nickel–cobalt–aluminum (NCA) lithium-ion batteries. Validated by 7 years of on-orbit data from a specific MEO satellite, the core conclusions are as follows.

1. NCA-type cells are suitable for supporting long-duration MEO orbital service under matched operation schemes. No battery degradation exceeding the measurement capability has been detected after seven years of on-orbit running, which provides a preliminary in-orbit data reference for the satellite's 10–15-year design life.
2. The assessment method and model are reliable. To address the challenge of incomplete charge–discharge cycles, an assessment method based on "discharge capacity vs. cut-off voltage" was established. Combined with the Random Forest and XGBoost algorithms, the mean squared error is better than 0.003 V^2. Although minor degradation is masked by the 2 mV AD sampling error, the predicted discharge voltage for the 20th eclipse season (end of design life) is 33 V, which is far higher than the 27 V EOL threshold, implying that the battery is likely to satisfy the full design service life.
3. Regarding data gaps, the 7-year dataset covering 14 eclipse seasons in this study fills the gap in long-term on-orbit data for MEO satellite batteries, providing a measured reference for subsequent model selection, management optimization, and life assessment.

Subsequent long-term on-orbit tracking and observation will be carried out to record the voltage variation characteristics after the cumulative degradation of the batteries exceeds the AD sampling error threshold. The prediction model will be further optimized to deliver more comprehensive technical support for the reliability evaluation of energy storage systems on medium- and high-orbit spacecraft.

Author Contributions: Conceptualization, H.L. and C.K.; methodology, H.L.; software, H.L.; validation, H.L. and C.K.; resources, B.L. and S.L.; writing—original draft preparation, C.K.; writing—H.L. and C.K.; visualization, Q.Z. and S.J. All authors have read and agreed to the published version of the manuscript.

Funding: This research received no external funding.

Data Availability Statement: Due to the strict confidentiality agreement signed between us and our cooperation partners for the data involved in this study, the relevant information contains sensitive commercial or technical content. Constrained by legal requirements and the terms of the confidentiality agreement, we are unable to make these data publicly available.

Conflicts of Interest: The authors declare no conflict of interest.

Abbreviations

The following abbreviations are used in this manuscript:

MEO	Medium Earth Orbit
NCA	$LiNiCoAlO_2$
LEO	Low Earth Orbit
DOD	Depth of Discharge
ICA	Incremental Capacity Analysis

References

1. Zheng, Y.; Jun, I.; Tu, W.; Shprits, Y.Y.; Kim, W.; Matthiä, D.; Meier, M.M.; Tobiska, W.K.; Miyoshi, Y.; Jordanova, V.K.; et al. Overview, progress and next steps for our understanding of the near-earth space radiation and plasma environment: Science and applications. *Adv. Space Res.* **2024**, in press. [CrossRef]
2. Kohani, S.; Zong, P. LEO constellation design for regional coverage based on the safety of van allen belt radiation. *J. Space Saf. Eng.* **2018**, *5*, 203–208. [CrossRef]
3. Wu, J.; Deng, L.; Praks, J.; Anger, M.; Oleynik, P.; Hajdas, W.; Wang, J.-D.; Zhang, S.-Y.; Zhou, B.; Zeng, L.; et al. CORBES: Radiation belt survey with international small satellite constellation. *Adv. Space Res.* **2025**, *75*, 6635–6652. [CrossRef]
4. Chen, X.; Ge, M.; Männel, B.; Schuh, H. Analysis of periodic terms in the DYB frame for the solar radiation pressure model of BDS-3 MEO satellites. *GPS Solut.* **2025**, *29*, 90. [CrossRef]

5. Tao, H.; Li, Z.; Huang, K.; Cui, J.; Li, Y. Study on the Optimization Method of Space Debris Orbit Prediction Based on Time Deviation Correction. *Infrared Laser Eng.* **2025**, *54*, 20250141-1.
6. Yang, X.; Tang, Z.; Yang, Y.; Wei, C.; Liu, Y.; Peng, Z.; Li, H.; Peng, Y.; Liu, Q.; Ge, L.; et al. Design and Evaluation of a Monitoring Instrument for the High-Energy Proton and TID Effects in LEO. *Space Sci. Rev.* **2024**, *220*, 33. [CrossRef]
7. Xiao, T.; Lei, Z.; Ma, T.; Fu, W.; Peng, C.; Zhang, H.; Fu, Z.; Song, H.; Guo, D.; Zhong, X.; et al. Influence of 300 MeV High-Energy Proton Irradiation on β-Ga2O3 Solar-Blind Ultraviolet Photodetector. *IEEE Trans. Electron Devices* **2025**, *72*, 6056–6060. [CrossRef]
8. Xi, C.X.; Liu, Y.; Lin, B.; Wang, X.; Jiang, G.; Kong, C. Radiation-resistant design of triple-junction gallium arsenide solar cell arrays for high-orbit satellites. *Acta Energ. Solaris Sin.* **2022**, *43*, 9–13. [CrossRef]
9. Qi, F.; Li, Y. *Manned Spacecraft Technology*, 2nd ed.; National Defense Industry Press: Beijing, China, 2003.
10. Maral, G.; Bousquet, M.; Sun, Z. *Satellite Communications Systems: Systems, Techniques and Technology*, 6th ed.; Wiley: Hoboken, NJ, USA, 2019.
11. Patel, M.R. *Spacecraft Power Systems*; CRC Press: Boca Raton, FL, USA, 2004.
12. Liao, J.; Jiang, Y.; Liao, H.; Xiao, D.-E.; Yuan, J.; Yang, Z.; Li, J.; Luo, S. Investigation on the effects of shadow on output performance and thermal characteristic of the solar array on stratospheric aerostat. *Energy* **2019**, *182*, 765–776. [CrossRef]
13. Wang, F.; Zhai, Z.; Di, Y.; Zhao, Z.; Chen, X. Physics-informed neural network for satellite battery degradation estimation based on an extreme segment data within 2 min. *IEEE Trans. Ind. Electron.* **2025**, *72*, 9748–9757. [CrossRef]
14. Chapel, L.; Picot, A.; Lacressonniere, F.; Maussion, P. Contribution to a review of lithium-ion batteries diagnostic methods for space applications. In *2023 IEEE 14th International Symposium on Diagnostics for Electrical Machines, Power Electronics and Drives (SDEMPED)*; IEEE: Piscataway, NJ, USA, 2023.
15. He, P.; Kong, C.J.; Zhang, Q.; Xi, C.X.; Liu, C.X.; Liu, E.Q.; Chen, T.M. On-orbit characteristic analysis of lithium cobalt oxide batteries for medium and high-orbit satellites. *Chin. J. Power Sources* **2023**, *47*, 1294–1297.
16. Chen, X.; Wang, S.; Zhang, H. Research on normalized diagnosis method for output current of LEO satellite solar array. 9th International Symposium on Test Automation & Instrumentation (ISTAI 2022). *IET Conf. Proc.* **2022**, *2022*, 280–286. [CrossRef]
17. Chen, Z.; Duo, G.D.; Shen, J.W.; Shen, S.Q.; Liu, Y.; Wei, F.X. State of health estimation for lithium-ion batteries based on incremental capacity analysis and VMD-GWO-KELM. *Energy Storage Sci. Technol.* **2025**, *14*, 2476–2487.
18. Song, Y.; Peng, Y.; Liu, D. Model-based health diagnosis for lithium-ion battery pack in space applications. *IEEE Trans. Ind. Electron.* **2020**, *68*, 12375–12384. [CrossRef]
19. Zhang, H.; Gui, X.; Zheng, S.; Lu, Z.; Li, Y.; Bian, J. BatteryML: An Open-source Platform for Machine Learning on Battery Degradation. In Proceedings of the International Conference on Learning Representations 2024 (ICLR 2024), Vienna, Austria, 7–11 May 2024.
20. Zhang, H.; Li, Y.; Zheng, S.; Lu, Z.; Gui, X.; Xu, W.; Bian, J. Battery lifetime prediction across diverse ageing conditions with inter-cell deep learning. *Nat. Mach. Intell.* **2025**, *7*, 270–277. [CrossRef]
21. Li, Y.; Zhang, H.; Gui, X.; Chen, Z.; Li, Y.; Chi, X.; Zhou, Q.; Zheng, S.; Lu, Z.; Xu, W.; et al. Chemistry-aware battery degradation prediction under simulated real-world cyclic protocols. *arXiv* **2025**, arXiv:2504.03701.
22. *GJB 9741-2020*; Specification for Lithium-Ion Battery Packs of Spacecraft. General Armaments Department of the People's Republic of China, China Standards Press: Beijing, China, 2020.
23. Tran, T.T.; Phan, N.Q.; Huynh, H.X. Random Forest Model Parameters Optimization. In *International Conference on Intelligent Systems and Data Science*; Springer Nature: Singapore, 2024.
24. Ghimire, B.R.; Maharjan, B.; Sharma, B.K.; Poudel, S.; Mishra, B.; Shahi, T.B. Mapping forest loss and encroachment drivers using remote sensing data and random forest classification. *Spat. Inf. Res.* **2025**, *33*, 17. [CrossRef]
25. Cepero-Pérez, N.; Moreno-Espino, M.; Morales, E.F.; López-González, A.; Yáñez-Márquez, C.; Pavón, J. A proactive approach for random forest: N. Cepero-Pérez et al. *Appl. Intell.* **2025**, *55*, 432.
26. Priya Varshini, A.G.; Anitha Kumari, K.; Ramakrishnan, S. Enhancing software effort estimation with random forest tuning and adaptive decision strategies. *Sci. Rep.* **2025**, *15*, 34053. [CrossRef] [PubMed]
27. van Geffen, F.; Hnsch, R.; Demir, B.; Kruse, S.; Herzschuh, U.; Heim, B. A Benchmark Dataset for Sentinel-2 Based Forest Type Classification in the Siberian Summergreen-Evergreen Forest Transition Zone. *IEEE J. Sel. Top. Appl. Earth Obs. Remote Sens.* **2025**, *18*, 18509–18527. [CrossRef]
28. Xing, J.; Liu, S.; Li, J. Medal Prediction Analysis Based on Random Forest and DID Models. In *2025 IEEE 3rd International Conference on Image Processing and Computer Applications (ICIPCA)*; IEEE: Piscataway, NJ, USA, 2025.
29. Martins, W.; Bagesteiro, L.B.; Weber, T.O.; Balbinot, A. FPGA-based Implementation of Random Forest Classifier for sEMG Signal Classification. In *2024 46th Annual International Conference of the IEEE Engineering in Medicine and Biology Society (EMBC)*; IEEE: Piscataway, NJ, USA, 2024.
30. Kanimozhi, J.K.; Bavya, G.; Kalyanasundaram, P.; Anitha, P.; Geetha, R.; Loganathan, E. Evaluating the Effectiveness of Random Forest+ XGBoost versus Support Vector Machines in Achieving High Accuracy and Precision for Breast Cancer Classification. In *2025 5th International Conference on Soft Computing for Security Applications (ICSCSA)*; IEEE: Piscataway, NJ, USA, 2025.

31. Uyar, S.G.K.; Ozbay, B.K.; Dal, B. Interpretable building energy performance prediction using XGBoost Quantile Regression. *Energy Build.* **2025**, *340*, 115815. [CrossRef]
32. Alsulamy, S. Predicting construction delay risks in Saudi Arabian projects: A comparative analysis of CatBoost, XGBoost, and LGBM. *Expert Syst. Appl.* **2025**, *268*, 126268. [CrossRef]
33. Zhao, X.; Zhang, P.-F.; Zhang, D.; Zhao, Q.; Tuerxunmaimaiti, Y. Prediction of interlaminar shear strength retention of FRP bars in marine concrete environments using XGBoost model. *J. Build. Eng.* **2025**, *105*, 112466. [CrossRef]
34. Mustaffa, Z.; Sulaiman, M.H. Advanced forecasting of building energy loads with XGBoost and metaheuristic algorithms integration. *Energy Storage Sav.* **2025**, *4*, 421–438. [CrossRef]
35. Zhang, L.; Lu, G.; Yan, X.; Xia, P.; Chen, Z.; Wu, D. A differential evolution optimized hybrid XGBoost for accurate carbon emission prediction. *Environ. Model. Softw.* **2025**, *193*, 106627. [CrossRef]

Disclaimer/Publisher's Note: The statements, opinions and data contained in all publications are solely those of the individual author(s) and contributor(s) and not of MDPI and/or the editor(s). MDPI and/or the editor(s) disclaim responsibility for any injury to people or property resulting from any ideas, methods, instructions or products referred to in the content.